SUPPLEMENTARY INFORMATION

Cubic-$Zn_{1-x}Mn_xTe$ optical modes across the phonon and phonon-polariton regimes

M. Mina,[1] A. Elmahjoubi,[2] T. Ngulezhu,[1,3] S. Thiam,[1] A. V. Postnikov,[1] T. Tite,[1] P. Bourges,[2] F. Bourdarot,[4] N. Biniskos,[4] A. Polian,[5] Y. Le Godec,[5,6] N. Guignot,[6] J.-P. Itié,[6] S. Diliberto,[7] S. Michel,[7] A. Maillard,[8] A. En Naciri,[1] L. Broch,[1] P. Franchetti,[1] K. Strzałkowski[3] and O. Pagès[1,a]

[1] Université de Lorraine, LCP-A2MC, F-57000 Metz, France
[2] Laboratoire Léon Brillouin, CEA-CNRS, Saclay, France
[3] Institute of Physics, Faculty of Physics, Astronomy and Informatics, Nicolaus Copernicus University in Toruń, ul. Grudziądzka 5, 87-100 Toruń, Poland
[4] Université Grenoble Alpes, CEA, IRIG, MEM, MDN, F-38000 Grenoble, France
[5] Institut de Minéralogie, de Physique des Matériaux et de Cosmochimie, Sorbonne Université — UMR CNRS 7590, F-75005 Paris, France
[6] Synchrotron SOLEIL, L'Orme des Merisiers Saint-Aubin, BP 48 F-91192 Gif-sur-Yvette Cedex, France
[7] Université de Lorraine, CNRS, IJL, F-57000, Metz, France
[8] Université de Lorraine, CentraleSupélec, LMOPS, F-57000 Metz, France

([a] Author to whom correspondence should be addressed: olivier.pages@univ-lorraine.fr)

Supplementary information (prefixed S) reports on additional experimental and theoretical data further supporting the discussion of the lattice structure (Sec. SI) and dynamics (Sec. SII) of $Zn_{1-x}Mn_xTe$ taken in the zb-phase, in relation to X-ray diffraction (XRD) and Raman scattering (RS), respectively. In the latter case both experimental and theoretical data are reported, concerned with backward/mTO-like and forward/PP-like Raman signals, and with the intra-bond LO-coupling within the Zn-Te dual optical mode of zb-$Zn_{1-x}Mn_xTe$, respectively.

SI. $Zn_{1-x}Mn_xTe$ lattice structure

Raw $Zn_{1-x}Mn_xTe$ XRDiffractograms obtained at minor (x=0.12) and large (x=0.37) alloying at the PSICHÉ beamline of SOLEIL synchrotron using the 0.3738 Å radiation at nearly ambient pressure by inserting finely ground powders inside a diamond anvil cell is displayed in Fig. S1. Au and Ne are used for pressure calibration and as the pressure transmitting medium, respectively. An additional powder XRDiffractogram related to large Mn content (x=0.67) was separately measured at ambient pressure in laboratory conditions using the 1.541 Å Cu Kα line (not shown). Sharp diffraction peaks, attesting a high crystal quality, indicate that all studied samples crystallize in the same zincblende (zb) structure as ZnTe. The individual XRDiffraction peaks in Fig. S1 are labelled accordingly via their (hkl) Miller's indices.

SII. $Zn_{1-x}Mn_xTe$ lattice dynamics

1. Backward-RS

Fig. S2 displays the full series of cross-polarized backward-RS spectra taken at the same sample spot with the 632.8 nm laser line across the zb-phase of $Zn_{1-x}Mn_xTe$ ($x \leq 0.7$) depending on the azimuth angle α between the incident polarization ($\vec{e}_i$) and the $[\bar{1}10]$ crystal axis taken as an arbitrary reference, step-increased by 20° until completing a full revolution (over 360°) at the sample surface. The reported symmetry analysis at x=0.37 in the inset of Fig. 2 refers to the α-dependence of the normalized (to the largest signal) Raman intensity (area) of the main ZnTe-like peak (modeled as a

Lorentzian/Gaussian function) in crossed ($\perp$, filled symbols) and parallel ($\parallel$, hollow symbols) polarizations of the incident ($\vec{e}_i$) and scattered ($\vec{e}_s$) lights. The Zn-Te and Mn-Te Raman intensities exhibit the same α-dependence corresponding to the theoretical quatrefoil Greekcross-like ($\perp$) and bilobed butterfly-like ($\parallel$) motifs axed $[\bar{1}10]$ and $[001]$, as ideally expected. Similar motifs are observed at x=0.12 (Fig. S2g) and x=0.67 (Fig. S2h). So, the lower/main Zn-Te and upper/minor Mn-Te Raman peaks consist of genuine mTO modes. The raw cross-top/parallel-bottom polarized Raman spectra collected at all studied x values (0.12, 0.37, 0.67) are displayed in Fig.S2. In each panel, the extreme (top and bottom) curves, referring to the same α addressed at the start and at the end of the revolution, help to appreciate the stability of the laser source across the full α-revolution.

2. Forward-RS

Fig. S3 displays a selection of cross-polarized forward-RS spectra obtained at various scattering angles θ with zb-$Zn_{0.33}Mn_{0.67}Te$ using the 632.8 nm laser line at quasi normal incidence/detection across parallel (110)-oriented crystals faces obtained by cleavage. The specified θ per spectrum are estimated so that the corresponding θ-dependent Raman scan line crosses the q-dependent zb- zb-$Zn_{0.33}Mn_{0.67}Te$ PP-RCS (comparable to that reported for x=0.37 in Fig. 3) exactly at the experimentally observed PP^- (small θ) or PP^{int+} (large θ) frequencies. By decreasing θ, the PPs progressively soften from their native Zn-Te and Mg-Te mTO modes. The PP^- mode hardly departs from its native mTO^{Zn}_{Zn-Te} mode as long as $\theta \geq$0.95° (Fig. S3) and then suddenly emerges as a distinct feature downshifted (frequency aspect) far below (by as much as ~50 cm^{-1}) the mTO^{Zn}_{Zn-Te} mode at $\theta \leq$0.85° (Fig. S3). No intermediate stage is observed. This is consistent with PP^- suffering a massive Raman extinction (intensity aspect) when it gets massively photon-like on crossing the photon asymptotes, which precisely occurs at the critical θ value θ_c~0.90° (Fig. 3). Remarkably, θ_c is also critical with respect to the PP^{int+} mode, subject to a broad↔sharp transition (linewidth aspect) at this limit (Fig. S3). This cannot be merely fortuitous, proving on an experimental basis that the latter transition can be traced back to the crossing of the photon-like asymptotes. The θ_c-coincidence affecting the PP^- and PP^{int+} modes is presumably intrinsic to zb-$Zn_{1-x}Mn_xTe$ alloying since it is independently observed with zb-$Zn_{0.63}Mn_{0.37}Te$ (Fig. 4).

Fig. S4 shows the raw forward-RS cross-polarized spectra at minimum scattering angle (θ~0°) behind the reported PP^- symmetry analysis at x=0.37 (Fig. 4, inset) and x=0.67 (Fig. S3, inset) using the 632.8 nm laser line. Similar spectra for x=0.12 complete the series. At a given x, the forward-RS PP-symmetry analysis is done at the same sample spot as the backward-RS mTO-symmetry analysis in Fig. S2. The specified α values do correspond. The PP^- Raman intensity in its α-dependence exhibits the same Greekcross-like motif (inset of Fig. 4, filled symbols) as that of the native mTO^{Zn-Te}_{Zn-Te} mode (inset of Fig. 2, filled symbols) attesting that they both consist of genuine TO modes. More generally, all three PP^-, PP^{int-} and PP^{int+} follow the same Raman selection rules depending on α (as apparent at any x in Fig. S4) attesting their identical (PP) nature.

3. Inter-bond LO-coupling – simplified two-oscillator MREI-like description

In the main text the inter-bond LO-coupling in $Zn_{1-x}Mn_xTe$ with zb-phase artificially expanded across the entire composition domain is treated in full by using the nominal three-oscillator percolation-type approach, referring to the native $\{mTO^{Zn}_{Zn-Te}, mTO^{Mn}_{Zn-Te}, mTO_{Mn-Te}\}$ modes behind the LO modes. The corresponding oscillator fractions $f_p(x)$ are listed in methods. A simplified MREI-like two-oscillator $\{mTO_{Zn-Te}, mTO_{Mn-Te}\}$ description is achieved by merging the percolation-type mTO_{Mn-Te}–mTO^{Zn}_{Zn-Te} duo into a unique MREI-like mTO_{Zn-Te} oscillator with fraction $f_{Zn-Te}(x) = 1 - x$. The remaining Mn-Te oscillator, already of the MREI-type, is represented in the crystal with fraction $f_{Mn-Te}(x) = x$. The corresponding two-mode uncoupled-$\{LO_{Zn-Te}, LO_{Mn-Te}\}$ and coupled-$\{LO^-, LO^+\}$ RCS are displayed in Fig. S5, using a minimum phonon damping (1 cm^{-1}). The E_L-coupling is manifested by a strong LO repulsion at the resonance (x~0) due to a massive $LO_{Zn-Te} \rightarrow LO_{Mn-Te}$ transfer of oscillator strength, reflected in the LO^- (minor) and LO^+ (dominant) Raman intensities (Fig.

S5-top, thickness of curves), in line with observed trends within the three-oscillator scheme (Fig. 5). The simplified two-oscillator scheme is, notably useful to compare on equal footing zb-$Zn_{1-x}Mn_xTe$ with zb-$Cd_{1-x}Zn_xTe$ and zb-$Ga_{1-x}In_xAs$, earlier treated in the same (MREI-like) way[29]. The comparison involves the dimensionless parameter τ (Fig. S5c), introduced in the main text, representing the amount of Zn-Te/Mn-Te mixing per coupled-LO mode depending on x. The full treatment, outlined in the main text offering the access to τ, is detailed in Ref. 29, referring specifically to Eqs. 3-to-5 therein. Remarkably, near the resonance ($x\sim0$), a higher mixing is achieved for zb-$Zn_{1-x}Mn_xTe$ ($\tau_{max}\sim0.5$ at $x\sim0.10$) than for $Cd_{1-x}Zn_xTe$ and zb-$Ga_{1-x}In_xAs$ ($\tau_{max}\sim0.4$ at $x\sim0.05$) – Ref. 29 (Fig. 7d therein).

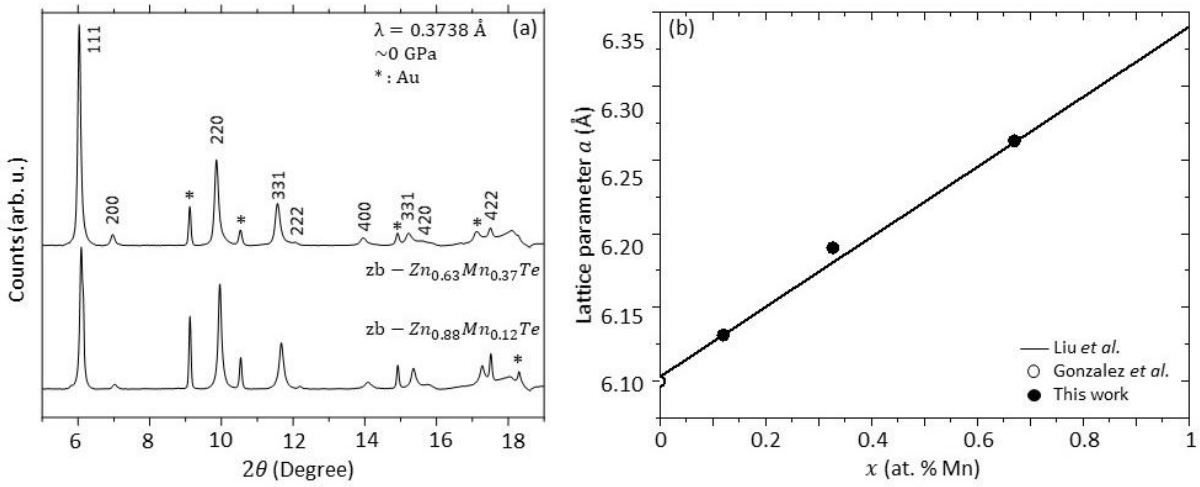


Figure S1. $Zn_{1-x}Mn_xTe$ crystal structure. (a) Powder X-ray diffractograms recorded at nearly ambient pressure on the PSICHÉ beamline of synchrotron SOLEIL with the 0.3738 Å radiation at x=0.12 and 0.37. The diffraction lines due to Au used for pressure calibration are indicated. The individual peaks are labeled using the (hkl) Miller indices of the corresponding diffraction planes in the zincblende-zb structure. **(b)** $a(x)$ dependence (symbols) derived from the lattice parameter a and the composition x independently measured in laboratory by powder X-ray diffraction with the Cu K-alpha radiation at ambient pressure and by applying the inductively coupled plasma-optical emission spectroscopy method to powders, respectively. The linear $a(x)$ variation found by Liu et al.[15] using epitaxial layers is added for comparison.

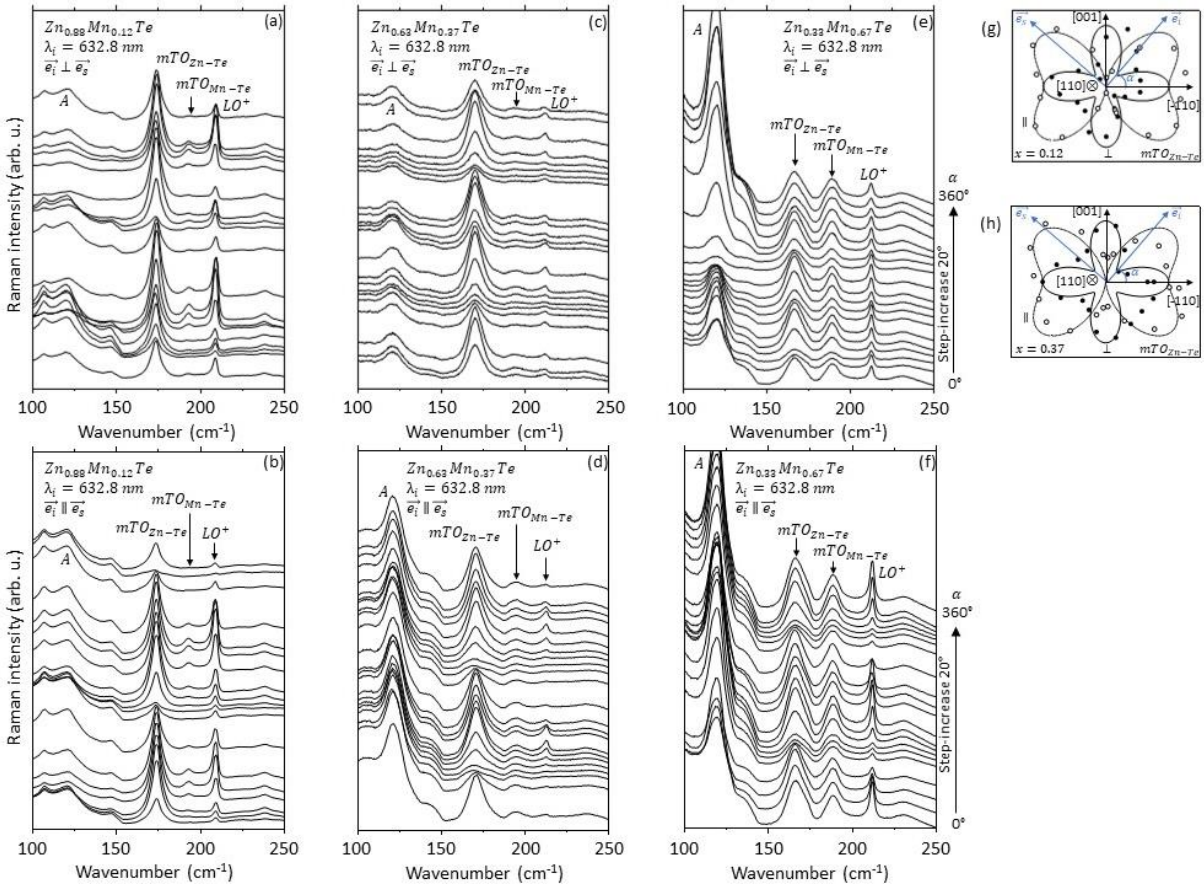


Figure S2. Polarized $Zn_{1-x}Mn_xTe$ mTO backward-RS spectra taken with the incident laser excitation λ_i =632.8 nm. Cross (top, ⊥) and parallel (down, ∥) polarized $Zn_{1-x}Mn_xTe$ mTO backward-RS spectra excited at the same sample spot of (110)-cleaved crystal faces depending on the azimuth angle α between the incident polarization ($\vec{e}_i$) and the $[\bar{1}10]$ crystal axis across the zb-phase, as sketched out (right). **(a/b)** x=0.12. **(c/d)** x=0.37. **(e/f)** x=0.67. **(g/h).** Corresponding experimental (symbols) vs. theoretical (curve) Greekcross- (⊥) and butterfly-like (∥) α-variations of the Zn-Te Raman intensity at small (x=0.12, g) and large (x=0.67, h) alloying. Corresponding data at moderate alloying (x=0.67) are shown in Fig. 2d. A denotes acoustic modes.

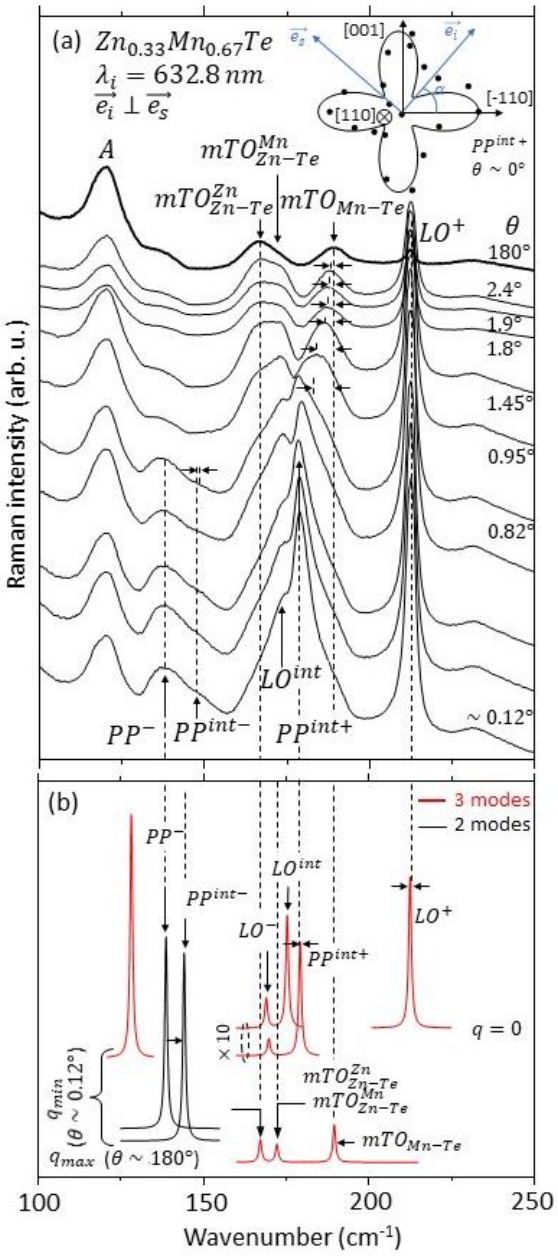


Figure S3. $Zn_{0.33}Mn_{0.67}Te$ forward-RS spectra across the phonon-polariton regime. **(a)** Cross-polarized $Zn_{0.33}Mn_{0.67}Te$ forward-RS PP spectra depending on the scattering angle θ inside the crystal, taken with the incident laser excitation λ_i =632.8 nm. The corresponding backward-RS spectra taken at the same crystal spot in the native mTO regime of the PPs is added (top/thick curve), for reference purpose. **Inset.** $Zn_{0.63}Mn_{0.67}Te$ PP^{int+} Raman intensity at θ_{min}~0° as a function of the azimuth angle α (as sketched out in Fig. 2) in crossed (filled symbols) polarizations ($\vec{e}_i \perp \vec{e}_s$). The raw data are shown in Fig. S4. The theoretical Greekcross-like (solid line) motif is superimposed, for comparison. **(b)** Nominal percolation-type 3-mode $\{2 \times (Zn-Te), 1 \times (Mn-Te)\}$ (red curves) PP-RCS at q_{min} (θ~12°) for the 632.8 nm laser line and corresponding asymptotic LO (q=0) and mTO (q_{max}) RCS. Truncated 2-mode $\{1 \times (Zn-Te), 1 \times (Mn-Te)\}$ descriptions are used to generate the uncoupled PP^- and PP^{int+} RCS (black curves) separately due to mTO^{Zn}_{Zn-Te} and mTO^{Mn}_{Zn-Te}, respectively, at q_{min} (see main text). Dashed guidelines are used to facilitate the comparison between the experimental (a) and theoretical (b) Raman frequencies. A small phonon damping (1 cm^{-1}) is used throughout to distinguish small and/or neighboring features. A denotes acoustic modes.

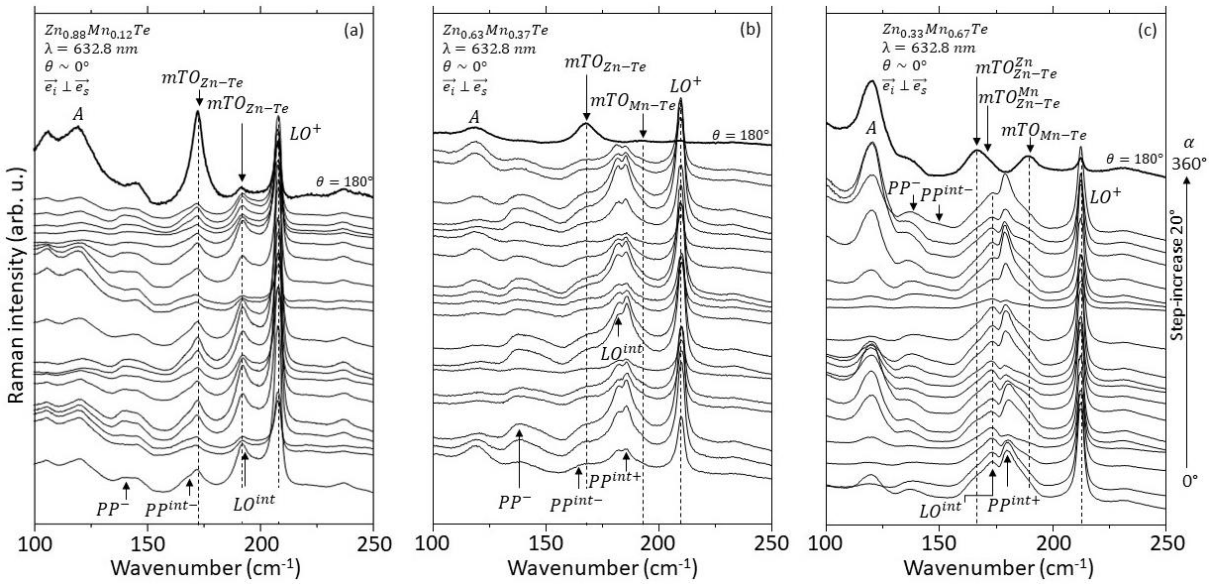


Figure S4. Polarized zb-$Zn_{1-x}Mn_xTe$ forward-RS spectra ($\theta \sim 0°$) taken with the incident laser excitation λ_i =632.8 nm. Cross-polarized (⊥) $Zn_{1-x}Mn_xTe$ forward-RS spectra excited at the same sample spots of (110)-cleaved crystal faces depending on the azimuth angle α between the incident polarization ($\vec{e}_i$) and the $[\bar{1}10]$ crystal axis across the zb-phase, as sketched out in Fig. S2g. **(a)** x=0.12. **(b)** x=0.37. **(c)** x=0.67. A denotes acoustic modes.

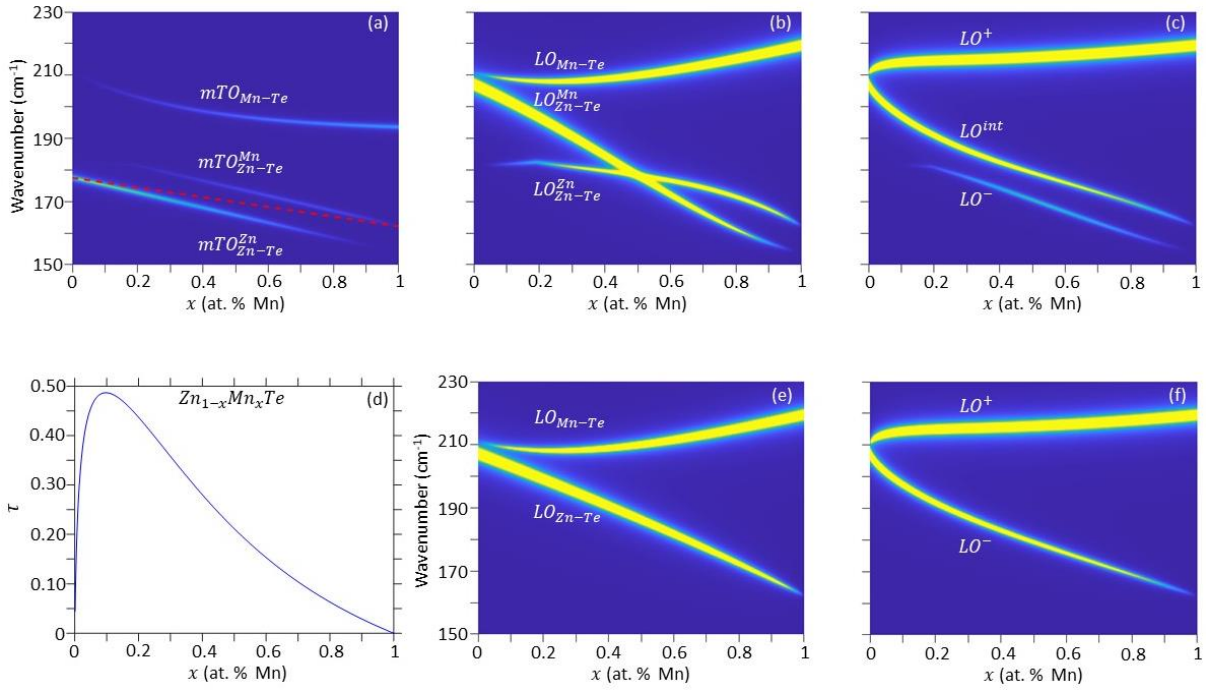


Figure S5. Theoretical LO-coupling in zb-$Zn_{1-x}Mn_xTe$ ($0 \leq x \leq 1$) – Percolation vs. MREI approaches. **Top.** Three-mode percolation model / frontal-2D views (the corresponding tilted-3D views are displayed in Fig. 5). **(a)** Mechanical-TO (mTO) RCS. **(b)** Uncoupled-LO RCS. **(c)** Coupled-LO RCS. **Bottom.** Two-mode MREI model. The percolation mTO Zn-Te duo is grasped into a unique MREI oscillator carrying the whole available Zn-Te oscillator strength – dotted/red line in panel (a). **(d)** Amount of coupling/mixing τ. **(e)** Uncoupled-LO RCS. **(f)** Coupled-LO RCS. A small phonon damping (1 cm^{-1}) is used throughout to distinguish small and/or neighboring features.